Near-field thermal radiation between doped silicon plates at nanoscale gaps

Mikyung Lim, Seung S. Lee, and Bong Jae Lee*

Department of Mechanical Engineering, Korea Advanced Institute of Science and Technology, Daejeon 305-701, South Korea

(Received 27 October 2014; revised manuscript received 29 April 2015; published 26 May 2015)

Radiative heat transfer can be significantly enhanced via photon tunneling through a nanometer-scale gap to the point that it exceeds the blackbody limit. Here we report quantitative measurements of the near-field thermal radiation between doped-Si plates (width = 480 μm and length = 1.34 cm). A novel MEMS-based platform enables us to maintain doped-Si plates at nanoscale gap distances that cannot be achieved by other methods. The measured radiative heat transfer coefficient was found to be 2.91 times greater than the blackbody limit at a 400-nm vacuum gap.

DOI: 10.1103/PhysRevB.91.195136

PACS number(s): 44.40.+a, 78.20.Ci

Since the 1960s, there have been a wide array of investigations demonstrating the near-field enhancements of radiative heat transfer between closely spaced objects [1–21]. Hargreaves [1] and Domoto *et al.* [2] first measured the near-field thermal radiation between two metallic surfaces separated down to a few micrometers at room temperature and at cryogenic temperatures, respectively. After Polder and Van Hove [3] provided a theoretical model for calculating the near-field thermal radiation between two planar surfaces based on the work by Rytov [4], theoretical works for the near-field thermal radiation between metallic [5] and dielectric [6] parallel surfaces have been explored. Furthermore, given that state-of-the-art MEMS/NEMS technology facilitates the fabrication of an electronic chip with doped-Si nanostructure, studies on nanoscale radiation between parallel doped-Si plates were also reported [7–10].

Despite a plethora of theoretical works, experimental demonstrations of near-field radiation are rather limited. Since Xu *et al.* [11] employed a modified scanning tunneling microscope tip to measure instances of radiative heat flux at nanometer scales, continuous efforts have been made to demonstrate near-field thermal radiation experimentally for relatively simple geometries [12–15]. However, spherical or pointlike geometries are not suitable for thermophotovoltaic (TPV) device applications, as the source area is inevitably limited, which in turn limits the power throughput of the device. For parallel-plate configurations, Hu *et al.* [16] and Ottens *et al.* [17] measured the near-field radiation between glass plates and sapphire plates, respectively, with a minimum vacuum gap of 1.6 μm near room temperature. Recently, Kralik *et al.* [18] demonstrated that near-field thermal radiation between metallic surfaces can be enhanced by nearly two orders of magnitude compared to the blackbody limit at cryogenic temperatures. However, in order to ensure practicality of the near-field TPV system, near-field thermal radiation between parallel plates must be measured first at elevated temperatures with submicron vacuum gaps. When maintaining such a short distance between parallel plates, a smaller apparatus can be advantageous because it avoids dust and parallelism issues. In this regard, Feng *et al.* [19] introduced MEMS technology for measuring the near-field thermal radiation between membranes; however, their results did not quantitatively agree with the theoretical predictions. Recent experimental study using MEMS nanobeam actuators resulted in quantitative agreements with the theory [20], but the near-field radiation between the nanoscale surfaces cannot be considered as that between plates. In addition, Ito *et al.* [21] measured the heat transfer between two quartz plates separated by fabricated pillars with a height of 500 nm; however, they could not distinguish near-field radiation from conduction.

In the present study we report quantitative measurements of the near-field radiation between parallel plates separated by nanoscale gaps using a novel MEMS-based platform. Phosphorous-doped-Si film is chosen as the source and the receiver because the optical properties of doped Si can be readily tuned by changing the doping concentration such that the surface plasmon can greatly enhance the near-field thermal radiation [10]. As shown in Fig. 1(a), in both source and receiver parts, a 600-nm-thick doped-Si film (doping concentration of $N = 8.33 \times 10^{19}$ cm^{-3} measured by a secondary ion mass spectrometry) is deposited on a fused-silica wafer with a 0.5-cm-wide trench. The receiver part is attached to a large Al heat sink maintained at 298 K, and the initial temperatures of the source/receiver parts and the heat sink are set to be 298 K for each measurement. A wire heater is attached to the source part to increase temperature of the source. Because conduction heat transfer from the wire heater to the receiver can occur only through the spacer that is over 0.5 cm apart from the receiver at the center, conducted heat through the spacer is eventually transferred to the Al heat sink located at the bottom of the receiver part rather than to the receiver film. As a result, conduction heat transfer from the source to the receiver is greatly suppressed due to the geometry of the proposed MEMS-based platform. Furthermore, a 20-μm-deep trench increases the separation distance between fused-silica surfaces, which can also hamper the near-field radiation between fused-silica substrates themselves.

In order to qualitatively demonstrate how the gap between the source and the receiver is controlled by applying a normal load, a finite element method (FEM) analysis is conducted on the MEMS-based platform with COMSOL Multiphysics®. As shown in Figs. 1(b) and 1(c), when a normal load is exerted on the spacer by pushing the jig positioned on the spacer, the part of Al heat sink just below the spacer is deformed more than the center part. Accordingly, the receiver part firmly attached to the heat sink deforms to a convex shape so that its displacement is also greater in the vicinity of the spacer than

*bongjae.lee@kaist.ac.kr

 ©2015 American Physical Society

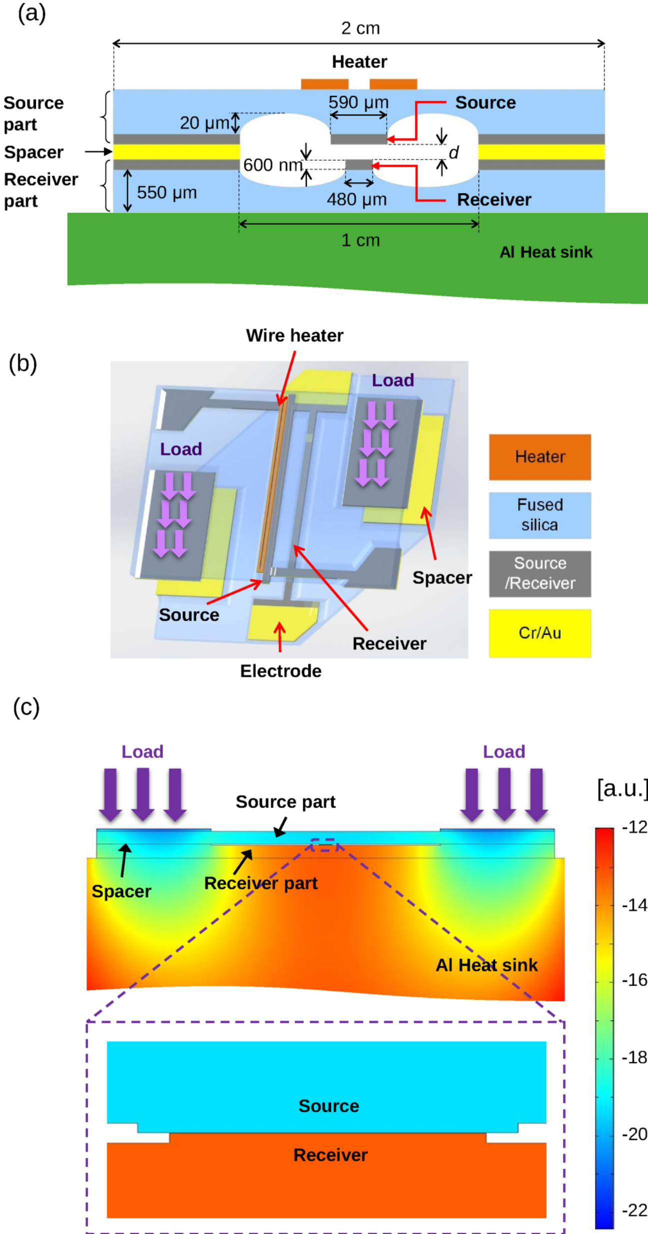

FIG. 1. (Color online) Proposed MEMS-based platform for measuring the near-field thermal radiation between doped-Si plates. (a) Cross-sectional view of the MEMS-based platform consisting of the source (i.e., doped-Si film of 590-μm width × 1.34-cm length × 600-nm thickness) and the receiver (i.e., doped-Si film of 480-μm width × 1.34-cm length × 600-nm thickness). The width of the source is intentionally designed to be wider than that of the receiver in order to assure that the receiver is fully covered by the source during the alignment. The actual heat transfer area was measured to be 480 μm × 1.34 cm by an optical microscope. (b) Three-dimensional schematic of the MEMS-based platform. (c) The displacement distribution in the source and the receiver parts under an arbitrary normal load.

at the center. On the other hand, the overall displacement of the source part is similar to that of the receiver part in the vicinity of the spacer because the source part is connected to the receiver part through the spacer. As a result, the local displacement of the source part at the center (i.e., the source film) is greater than the corresponding point in the receiver part (i.e., the receiver film), as clearly seen from Fig. 1(c). By this mechanism, the relative displacement of the source and the receiver (i.e., increment/decrement of the vacuum gap) can be varied by applying a normal load. By carefully adjusting the micrometer attached to the jig, the vacuum gap between the source and the receiver can be decreased as narrow as 400 nm.

The near-field thermal radiation between thin films or thin-film-coated media has been well understood [10,22–25]. In this work, the near-field thermal radiation between doped-Si films is calculated by the two-body formulation with modified reflection coefficients [10,23,25] using the frequency-dependent dielectric functions of doped Si [26] and fused silica [27], as briefly summarized below. Consider two doped-Si films with a thickness of d_f on semi-infinite fused-silica substrates, separated by a vacuum gap width d. The spectral radiative heat flux from the source (medium 1) to the receiver (medium 2) can be expressed as $q''_{\omega,1\rightarrow 2} = \sum_{\gamma=p,s}\int_0^\infty S^\gamma(\beta,\omega)d\beta$, where β is the parallel wave vector component and ω is the angular frequency. Here the superscript γ indicates the polarization index. The expression for $S^\gamma(\beta,\omega)$ is different for propagating and for evanescent waves in vacuum as [3]

$$S^\gamma_{\mathrm{prop}} = \frac{\Theta(\omega,T_1)}{\pi^2}\frac{\beta\left(1-|r^\gamma_{01}|^2\right)\left(1-|r^\gamma_{02}|^2\right)}{4\left|1-r^\gamma_{01}r^\gamma_{02}e^{i2k_{0z}d}\right|^2},$$
$$S^\gamma_{\mathrm{evan}} = \frac{\Theta(\omega,T_1)}{\pi^2}\frac{\beta\,\mathrm{Im}\left(r^\gamma_{01}\right)\mathrm{Im}\left(r^\gamma_{02}\right)e^{-2\mathrm{Im}(k_{0z})d}}{\left|1-r^\gamma_{01}r^\gamma_{02}e^{i2k_{0z}d}\right|^2}. \quad (1)$$

In the equations above, $k_{iz} = \sqrt{\omega^2/c_0^2\epsilon_i - \beta^2}$ is the normal wave vector component in the ith medium, Im( ) takes the imaginary part of a complex quantity, and $\Theta(\omega,T_1) = \frac{\hbar\omega}{\exp\{\hbar\omega/(k_B T_1)\}-1}$ is the mean energy of the Planck oscillator at the source temperature T_1, where $\hbar$ indicates the Planck constant divided by 2π and k_B is the Boltzmann constant. The functional expressions of r^γ_{01} and r^γ_{02} are obtained from Airy's formulas [28]

$$r^\gamma_{01} = \frac{r^\gamma_{0(1f)} + r^\gamma_{(1f)(1s)}e^{2ik_{(1f)z}d_f}}{1 + r^\gamma_{0(1f)}r^\gamma_{(1f)(1s)}e^{2ik_{(1f)z}d_f}},$$
$$r^\gamma_{02} = \frac{r^\gamma_{0(2f)} + r^\gamma_{(2f)(2s)}e^{2ik_{(2f)z}d_f}}{1 + r^\gamma_{0(2f)}r^\gamma_{(2f)(2s)}e^{2ik_{(2f)z}d_f}}, \quad (2)$$

where $r^\gamma_{0(1f)}$ and $r^\gamma_{(1f)(1s)}$ are the Fresnel reflection coefficients at the 0-1f interface (i.e., between vacuum and doped-Si film of the source part) and at the 1f-1s interface (i.e., between doped-Si film and fused-silica substrate of the source part), respectively. Likewise, $r^\gamma_{0(2f)}$ and $r^\gamma_{(2f)(2s)}$ represent the Fresnel reflection coefficients at the corresponding interfaces of the receiver part. The net heat flux q''_{net} between the source and the receiver can be calculated as $q''_{\mathrm{net}} = \int_0^\infty [q''_{\omega,1\rightarrow 2} - q''_{\omega,2\rightarrow 1}]d\omega$.

Figures 2(a) and 2(b) show photographs of the fabricated device. Because the electrical resistance of doped Si varies with temperature, the source and the receiver can function as a temperature sensor. In order to detect the temperature of only the source and the receiver [i.e., portion denoted by dashed line in Figs. 2(a) and 2(b), respectively], all of the connecting parts were coated with Cr/Au, whose electrical resistance is

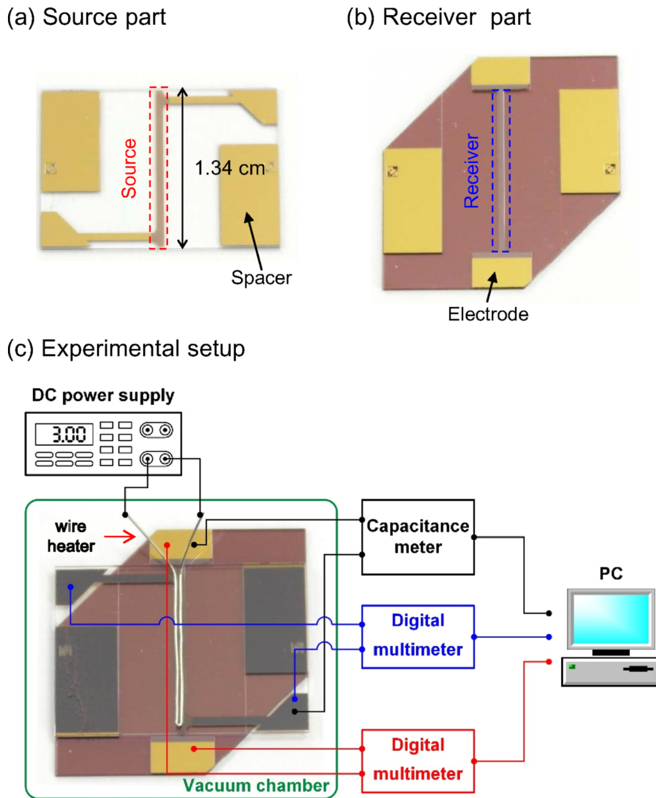

FIG. 2. (Color online) Fabricated MEMS-based platform and experimental setup. Photographs of the fabricated (a) source and (b) receiver parts. (c) Detailed experimental setup. The red line connects the receiver to a DMM, and blue line connects the source to a DMM. One electrode for each of the source and the receiver are connected to a capacitance meter to estimate the vacuum gap during the experiments. A U-shaped wire is connected to a dc power supply to increase the temperature of the source.

three orders of magnitude lower than that of doped Si. The root-mean-squared roughness of the deposited doped-Si film was measured to be 3.5 nm by an atomic force microscope; thus, the surface roughness does not significantly alter the vacuum gap distance. In addition, before assembling the source and receiver parts in a cleanroom environment, both surfaces of the source and the receiver were thoroughly examined with a three-dimensional optical surface profilometer to confirm the absence of dust. In order to neglect gas conduction from the source to the receiver, the experiment was conducted in a high vacuum chamber (pressure is less than 1×10^{-3} Pa).

Figure 2(c) describes the experimental setup. Real-time measurements of the capacitance between the source and the receiver allowed us to estimate the vacuum-gap width precisely. Because the MEMS-based platform in the vacuum chamber is connected to a capacitance meter via a vacuum feed-through, the capacitance measurement needs to be calibrated. Furthermore, the simultaneous measurement of the electrical resistance and capacitance also results in an additional increase in the measured capacitance due to the internal capacitance of digital multimeters (DMMs). Consequently, the capacitance measurement was calibrated with reference capacitors in a configuration identical to that used in the actual experiment to obtain the following relationship: $C_{\text{measured}} = C_{\text{actual}} + C_{\text{parallel}}$, where C_{measured} is the measured capacitance outside of the vacuum chamber and C_{actual} is the actual capacitance of the device. The capacitance C_{parallel}, containing the contribution of the parallel connection including the vacuum feed-through and the internal capacitance of DMMs, was found to be 153 ± 5 pF.

At the beginning of each measurement, a wire heater is Joule heated by a dc power supply at 3 V, and DMMs are used to measure the electrical resistances of the source and the receiver by the four-wire method. The measured resistance of the source and the receiver is then converted to temperature using a calibration factor; that is, the receiver resistance changes by $-27.4\ \Omega/\text{K}$ and the source resistance is 6480 Ω at 371 K. The receiver calibration factor of $-27.4\ \Omega/\text{K}$ with an error of $0.03\ \Omega/\text{K}$ is obtained from a linear fitting of 60 resistance data with respect to the measured temperature in the range of $294 < T < 303$ K [29].

In order to obtain the radiative heat transfer coefficient h_R, we initially converted the decreased receiver resistance to the increased receiver temperature. This value led to the estimation of the radiative heat transfer coefficient according to the conversion factor that is obtained from a FEM analysis using COMSOL Multiphysics® with built-in thermal conductivities of Si and silica, as briefly explained in the following.

Because the wire heater is placed in line on top of the source part as shown in Fig. 2(c), the temperature gradient along the surface of the source in the length direction can be neglected, suggesting that uniform near-field radiative transfer occurs from the source to the receiver. In addition, lengths of the source and the receiver are far greater than their width, such that the conduction loss to the electrodes at the edges of the receiver can be neglected. Therefore, we can conduct a FEM analysis simply for the two-dimensional structure shown in Fig. 1(a). During the simulation, an uniform heat flux is applied to the receiver film surface as a boundary condition (i.e., assigning h_R value). Because the gap between the source and the receiver ($<1\ \mu$m) is far smaller than the width of receiver (480 μm), the edge effect in the near-field radiation can be ignored. For a given h_R value, FEM simulation results in the corresponding receiver temperature increase. By repeating the simulation with different h_R values, the conversion factor is finally obtained to be 6.40 W/m^2 K for every 0.1 K increase in the receiver temperature, as shown in Fig. 3(a). Because the electrical resistance of receiver film is relevant to the average temperature of receiver film, we averaged the receiver temperature in the width direction from FEM simulation and use it when calculating the conversion factor.

It should be noted that the receiver temperature can also increase due to conduction from the wire heater, but this conduction contribution should be independent of the near-field radiation. In order to eliminate the conduction contribution from the measurements, we fitted the radiative heat transfer coefficient at $d = 980$ nm with theory. In other words, the near-field heat transfer coefficients h_R at other vacuum-gap distances were obtained from the relative increase in the receiver temperature from the reference datum at $d = 980$ nm.

The measured radiative heat transfer coefficients are plotted in Fig. 3(b). For vacuum-gap widths from 400 to 1030 nm, the radiative heat transfer coefficient is in excellent agreement

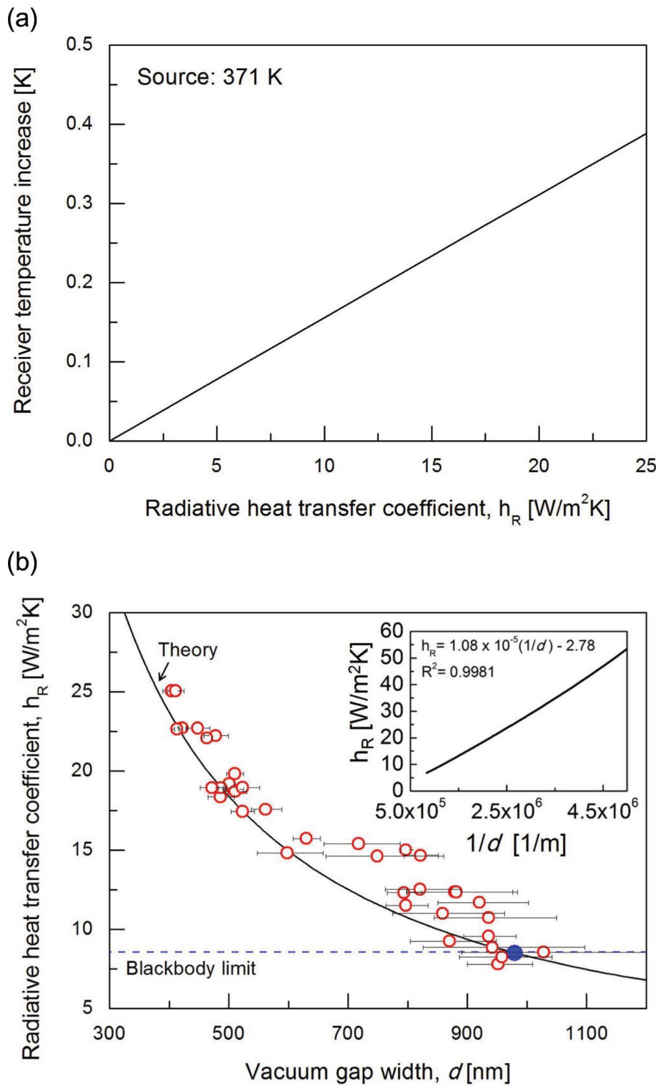

FIG. 3. (Color online) Near-field radiative heat transfer coefficient. (a) The increase in the receiver temperature as predicted by a COMSOL simulation with respect to the radiative heat transfer coefficient when the source temperature is fixed at 371 K. (b) The measured radiative heat transfer coefficients from $d = 400$ nm to $d = 1030$ nm (red open circles). The reference datum used to remove the conduction contribution is denoted with a blue filled circle. The vacuum gap width is estimated from the average value of capacitance during 10 s for each point and the standard deviation of the measured capacitance is denoted as an error bar in the vacuum gap. The black line represents the radiative heat transfer coefficient obtained from the two-body formulation with modified Fresnel coefficients. The inset describes the linearity between the calculated radiative heat transfer coefficient and the inverse of the vacuum-gap width.

with the two-body formulation. The maximum radiative heat transfer coefficient of 25.0 W/m^2 K is approximately 2.91 times greater than the blackbody limit. Such an enhancement is unprecedented for the near-field radiation between plates especially for above room temperature.

It is worthwhile to mention that for our MEMS-based platform, any further approximations or adjustments are not necessary when comparing the experimental data with the theoretical prediction. Because the separation distance is estimated from the capacitance measurement between entire surfaces of the source/receiver films, the obtained distance is simply the average gap distance. In addition, the average temperature increase is obtained from the electrical resistance change, which is then converted to the average radiative heat transfer coefficient. As discussed in Appendix C, the average radiative heat transfer coefficient is nothing but the radiative heat transfer coefficient at the average gap distance. Consequently, our MEMS-based platform inherently measures the average separation distance as well as the radiative heat transfer coefficient at the corresponding average gap. Therefore, a proximity approximation to account for nonparallelism is no longer needed.

Moreover, the proposed MEMS-based platform ensures no physical contact between any parts of the source and the receiver films during the measurements. This is crucial to properly measure the near-field thermal radiation because conduction heat transfer through physical contacts between the source and the receiver can result in huge increase in the total heat flux, which can be falsely regarded as an enhancement in thermal radiation. In addition, conduction heat transfer through contacts can also cause nonuniform temperature distribution on the source and the receiver films, yielding considerable deviations of the measured radiative heat flux from the theoretical value.

In summary, we report quantitative measurements of the near-field thermal radiation between nearly parallel plates at submicron gaps. The novel MEMS-based structure enabled us to maintain doped-Si plates down to 400 nm. The maximum radiative heat transfer coefficient of 25.0 W/m^2 K was approximately 2.91 times greater than the blackbody limit. In contrast to previous studies that used relatively simple geometries, the proposed MEMS-based platform can directly affect the future development of near-field TPV systems with high power throughput.

ACKNOWLEDGMENTS

This research was supported by Basic Science Research Program through the National Research Foundation of Korea (NRF) funded by the Ministry of Science, ICT and Future Planning (NRF-2012R1A1A1006186 and NRF-2013R1A1A2019816), civil military technology co-operation program (Grant No. 14-BR-SS-12), and the KAIST End Run Project program (Grant No. N01150142).

APPENDIX A: FABRICATION OF THE MEMS-BASED PLATFORM

As shown in Fig. 4(a), a 300-nm-thick poly-Si film was deposited and patterned on a fused-silica wafer by means of reactive ion etching (RIE). Using this poly-Si film as an etching mask, the fused-silica wafer was etched with a buffered oxide etchant at approximately 20 μm to create a groove on it [refer to Fig. 4(b)]. After removing the photoresist (PR) and the poly-Si etching mask as shown in Fig. 4(c), a phosphorous-doped-Si film was deposited onto the patterned fused-silica wafer and then patterned as the source/receiver [refer to Fig. 4(d)]. For the spacer shown in Fig. 4(e), Cr/Au film was deposited

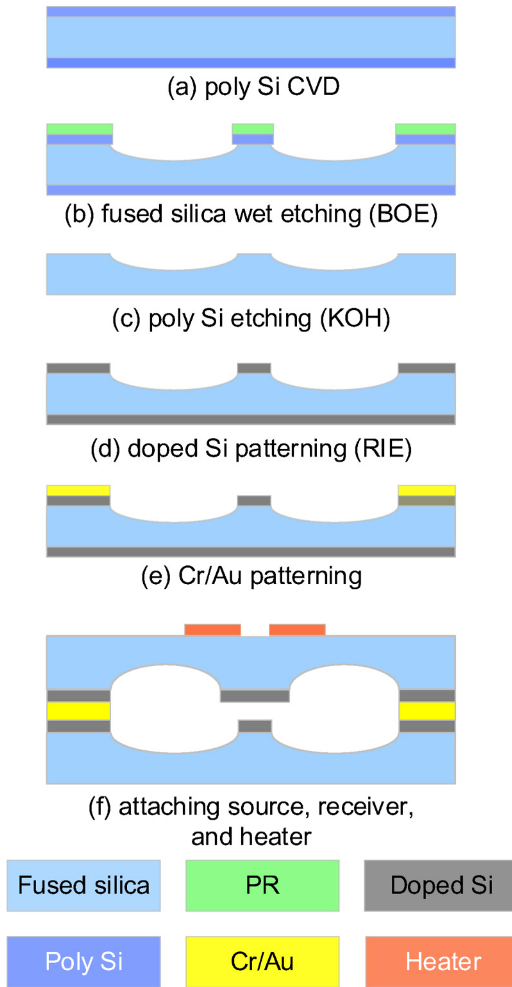

FIG. 4. (Color online) Fabrication processes of the MEMS-based platform.

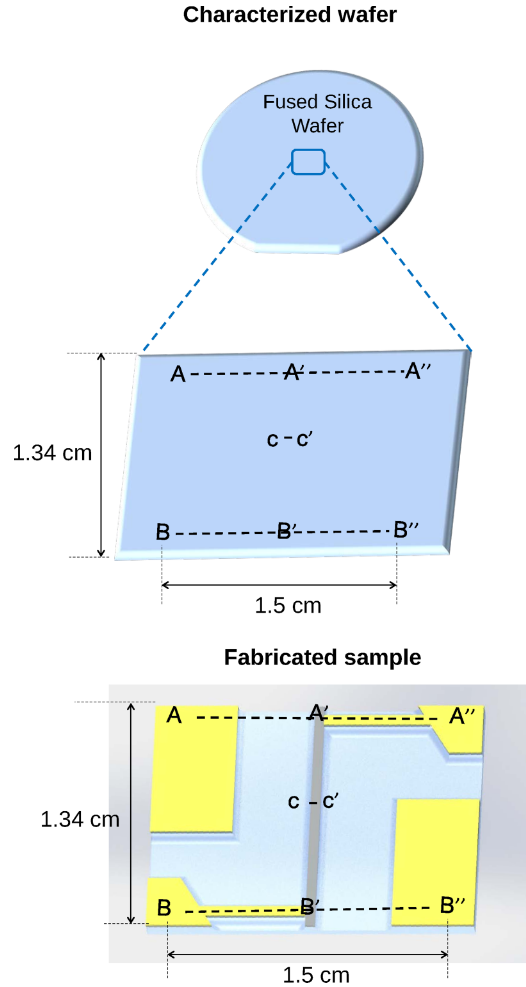

FIG. 5. (Color online) The direction of a bare fused-silica wafer.

and patterned by a lift-off process. In Fig. 4(f), the fabricated source and receiver parts were carefully aligned and assembled together. Finally, a wire heater was attached onto the source part for the experiment.

APPENDIX B: DEGREE OF INCLINATION/CURVATURE OF THE SOURCE/RECEIVER PARTS

A surface profile of a bare fused-silica wafer was measured to estimate the inclination/curvature of the source and the receiver parts based on the following two assumptions.

First, we assume that the surface profile (i.e., inclination and curvature) of a bare fused-silica wafer is the same as that of the fabricated sample. As can be seen from Figs. 4 and 5, doped-Si film was deposited on a fused-silica wafer for the source/receiver and the spacer by LPCVD (low pressure chemical vapor deposition) and then Cr/Au film was deposited only for the spacer with an *e*-beam evaporator. The thickness of doped-Si film and Cr/Au film was measured using a spectroscopic ellipsometer (M2000D, Woollam) and a surface profiler (Dektak-8, VEECO), respectively. It is found that the thickness variation of 900-nm-thick (targeted in the nanofabrication process) doped-Si/Cr/Au film over the entire area of 1.5 cm × 1.34 cm is less than 10 nm in total. Therefore, we can confirm that the thickness of the doped-Si/Cr/Au film is fairy uniform and the surface profile of a bare fused-silica wafer can be assumed to be the same as that of the doped-Si/Cr/Au-deposited fabricated sample.

The other assumption is that the spacers of the source/receiver parts are on the same plane. Figure 1(c) depicts that the source part and the receiver part make a plane contact with their spacers and they are tightly bonded. This means that the spacers are all on the same reference plane. For this reason, we set the spacer plane (including A-B and A″-B″ lines in Fig. 5) as the reference plane throughout the following discussion.

Based on the above assumptions, we can get a sense of how the source and the receiver films are tilted or curved by characterizing the inclination/curvature of a bare fused-silica wafer with respect to the reference plane.

In order to estimate the inclination of the source/receiver films in the length direction with respect to the spacer plane (i.e., reference plane including A-B and A″-B″ lines), surface profiles of the bare fused-silica wafer were measured as follows. Along the A-A′-A″ line, the A′ is 319 nm lower than the A-A″ line. However, along the B-B′-B″ line, the B′ is deviated 269 nm from the B-B″ line. Since A-B and

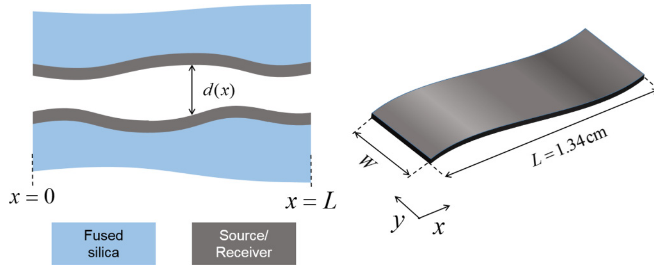

FIG. 6. (Color online) Schematic illustration of variation in the separation distance $d(x)$ along the source/receiver films.

A″-B″ lines are assumed to be on the reference plane, it can be concluded that the source/receiver planes are tilted about 50 nm from the reference plane. In addition, the result obtained from the surface profiler in A′-B′ direction suggests that 40 nm is deviated from being flat along the length direction (i.e., radius of curvature is 561 m).

When the flatness of the fused-silica wafer in direction c-c′ is considered, less than 2 nm is deviated from being flat along c-c′ direction over 590 μm. In addition, the c-c′ line is tilted less than 3 nm compared to the reference plane. Therefore, the inclination/curvature in c-c′ direction can be safely neglected.

Furthermore, if the source is heated up to 371 K, the difference between thermal expansion coefficients of the source film and fused silica substrate can result in small flexure. By measuring local height variations of the fabricated source film while being electrically heated (i.e., Joule heating) to 371 K, it is confirmed that the mismatch of thermal expansion coefficients of Si and fused silica can cause a height variation less than 50 nm in A′-B′ direction (measured by three-dimensional optical surface profilometer).

In summary, there exist 50 nm tilting and 40 nm deviation from being flat along the length direction, resulting in height variations of 65 nm compared to the reference plane for each source/receiver films. Thus, considering the variation of 50 nm caused by thermal expansion in the source, there would be *at worst* 180-nm gap variations between the source and the receiver films along the length of 1.34 cm.

APPENDIX C: AVERAGE SEPARATION GAP AND AVERAGE HEAT TRANSFER COEFFICIENT BETWEEN NONPARALLEL SURFACES

Let us consider two plates separated by $d(x)$ shown in Fig. 6. Because there is negligible tilting or curvature in the width direction (i.e., y direction), variation in the separation distance is considered along the length direction (i.e., x direction) only. In other words, d is treated as a function of x only. From the measured capacitance (C_m) between the entire surfaces of the source/receiver, the separation distance (d_m) was obtained from

$$C_m = \epsilon \frac{WL}{d_m}, \tag{C1}$$

where ϵ is the vacuum permittivity and W and L are width and length, respectively, of the source/receiver films.

Alternatively, the total capacitance between the source/receiver can also be calculated by integrating the differential capacitance dC over the entire surfaces of the source/receiver of area A:

$$C = \int_A dC. \tag{C2}$$

If the ratio of the plate length to the separation distance is larger than 130, the fringing effect can be neglected [30]. Furthermore, for the differential area dA, if the source/receiver can be considered as parallel-plate configuration, then dC can be expressed simply as

$$dC = \epsilon \frac{dA}{d(x)}. \tag{C3}$$

In the case of the fabricated MEMS-based platform, if we take the differential area $dA = W \times dx$ with $dx = 130\ \mu$m (i.e., 130 times of the maximum gap distance of 1 μm), there would be less than 2-nm-gap variation, which is negligible compared to $dx = 130\ \mu$m (see Appendix B for details). Therefore, we can safely apply Eqs. (C2) and (C3) to the MEMS-based platform if the differential area is taken approximately as 1/100 of the total length ($L = 1.34$ cm). Then, the total capacitance can be written as

$$C = \int \epsilon \frac{dA}{d(x)} = \int_0^L \epsilon \frac{W dx}{d(x)} = \epsilon W \int_0^L \frac{dx}{d(x)}. \tag{C4}$$

Comparing Eqs. (C1) and (C4) yields

$$\epsilon \frac{WL}{d_m} = \epsilon W \int_0^L \frac{dx}{d(x)}, \tag{C5}$$

and thus,

$$d_m = L \left[\int_0^L \frac{dx}{d(x)} \right]^{-1} = d_{\mathrm{avg}}. \tag{C6}$$

Consequently, the vacuum gap distance obtained from the capacitance measurement is nothing but the average distance.

Regarding the radiative heat transfer coefficient (h_R), its increment is predicted to be proportional to $1/d$ when the vacuum gap width varies from 200 to 1200 nm, as shown in the inset of Fig. 3(b). If we let h_R as $h_R\{d(x)\} = \frac{a}{d(x)} + b$, then the average radiative heat transfer coefficient along the plates can be calculated using Derjaguin approximation as [15,31]

$$h_{R,\mathrm{avg}} \times (WL) = \int_A h_R\{d(x)\} dA, \tag{C7}$$

and thus,

$$h_{R,\mathrm{avg}} = \frac{a}{L} \int_0^L \frac{dx}{d(x)} + b = \frac{a}{d_{\mathrm{avg}}} + b. \tag{C8}$$

It can be readily seen that the relation of $h_{R,\mathrm{avg}}$ in Eq. (C8) is identical to $h_R(d_{\mathrm{avg}})$, where d_{avg} is obtained from Eq. (C6); that is, the average radiative heat transfer coefficient is nothing but the radiative heat transfer coefficient at the average gap distance.

APPENDIX D: THE EFFECT OF THERMAL CONTACT (OR BOUNDARY) RESISTANCE

As a matter of fact, the increase in the receiver-film temperature depends on (i) thermal resistance of the receiver film (10^{-9} m^2 K W^{-1}); (ii) thermal resistance of the fused-silica

substrate (10^{-4} m^2 K W^{-1}); (iii) thermal boundary resistance between the doped-Si film and the fused-silica substrate (10^{-9}–10^{-8} m^2 K W^{-1}) [32,33]; and (iv) thermal contact resistance between the fused-silica substrate and the Al heat sink (10^{-6} m^2 K W^{-1}) [34]. Based on the order-of-magnitude analysis, it can be concluded that the thermal contact (or boundary) resistance hardly affects the measured temperatures of both source and receiver films.

[1] C. M. Hargreaves, Phys. Lett. A **30**, 491 (1969).
[2] G. A. Domoto, R. F. Boehm, and C. L. Tien, J. Heat Transfer **92**, 412 (1970).
[3] D. Polder and M. Van Hove, Phys. Rev. B **4**, 3303 (1971).
[4] S. M. Rytov, Y. A. Kratsov, and V. I. Tatarskii, *Principles of Statistical Radiophysics* (Springer, Berlin, 1987), Chap. 3.
[5] P.-O. Chapuis, S. Volz, C. Henkel, K. Joulain, and J.-J. Greffet, Phys. Rev. B **77**, 035431 (2008).
[6] J.-P. Mulet, K. Joulain, R. Carminati, and J.-J. Greffet, Microscale Thermophys. Eng. **6**, 209 (2002).
[7] F. Marquier, K. Joulain, J.-P. Mulet, R. Carminati, and J.-J. Greffet, Opt. Commun. **237**, 379 (2004).
[8] C. J. Fu and Z. M. Zhang, Int. J. Heat Mass Transfer **49**, 1703 (2006).
[9] S. Basu, B. J. Lee, and Z. M. Zhang, J. Heat Transfer **132**, 023302 (2010).
[10] M. Lim, S. S. Lee, and B. J. Lee, Opt. Express **21**, 22173 (2013).
[11] J.-B. Xu, K. Läuger, R. Möller, K. Dransfeld, and I. H. Wilson, J. Appl. Phys. **76**, 7209 (1994).
[12] A. Kittel, W. Müller-Hirsch, J. Parisi, S.-A. Biehs, D. Reddig, and M. Holthaus, Phys. Rev. Lett. **95**, 224301 (2005).
[13] A. Narayanaswamy, S. Shen, and G. Chen, Phys. Rev. B **78**, 115303 (2008).
[14] S. Shen, A. Narayanaswamy, and G. Chen, Nano Lett. **9**, 2909 (2009).
[15] E. Rousseau, A. Siria, G. Jourdan, S. Volz, F. Comin, J. Chevrier, and J.-J. Greffet, Nat. Photon. **3**, 514 (2009).
[16] L. Hu, A. Narayanaswamy, X. Chen, and G. Chen, Appl. Phys. Lett. **92**, 133106 (2008).
[17] R. S. Ottens, V. Quetschke, S. Wise, A. A. Alemi, R. Lundock, G. Mueller, D. H. Reitze, D. B. Tanner, and B. F. Whiting, Phys. Rev. Lett. **107**, 014301 (2011).
[18] T. Kralik, P. Hanzelka, M. Zobac, V. Musilova, T. Fort, and M. Horak, Phys. Rev. Lett. **109**, 224302 (2012).
[19] C. Feng, Z. Tang, J. Yu, and C. Sun, Sensors **13**, 1998 (2013).
[20] R. St-Gelais, B. Guha, L. Zhu, S. Fan, and M. Lipson, Nano Lett. **14**, 6971 (2014).
[21] K. Ito, A. Miura, H. Iizuka, and H. Toshiyoshi, Appl. Phys. Lett. **106**, 083504 (2015).
[22] A. I. Volokitin and B. N. J. Persson, Phys. Rev. B **63**, 205404 (2001).
[23] S.-A. Biehs, Eur. Phys. J. B **58**, 423 (2007).
[24] P. Ben-Abdallah, K. Joulain, J. Drevillon, and G. Domingues, J. Appl. Phys. **106**, 044306 (2009).
[25] M. Francoeur, M. P. Mengüç, and R. Vaillon, J. Phys. D: Appl. Phys. **43**, 075501 (2010).
[26] S. Basu, B. J. Lee, and Z. M. Zhang, J. Heat Transfer **132**, 023301 (2010).
[27] E. D. Palik, *Handbook of Optical Constants of Solids* (Academic, New York, 1985), Vol. 1.
[28] P. Yeh, *Optical Waves in Layered Media* (Wiley, New York, 1988), Chap. 4.
[29] See Supplemental Material at http://link.aps.org/supplemental/10.1103/PhysRevB.91.195136 for characterization of the fabricated source/receiver films.
[30] D. O. Ducu, R. J. Donahue, and J. B. Ghandhi, J. Eng. Gas Turb. Power **123**, 633 (2001).
[31] B. V. Derjaguin, I. I. Abrikosova, and E. M. Lifshitz, Q. Rev. Chem. Soc. **10**, 295 (1956).
[32] S.-M. Lee and D. G. Cahill, J. Appl. Phys. **81**, 2590 (1997).
[33] D. H. Hurley, M. Khafizov, and S. L. Shinde, J. Appl. Phys. **109**, 083504 (2011).
[34] F. P. Incropera, D. P. DeWitt, T. L. Bergman, and A. S. Lavine, *Principles of Heat and Mass Transfer* (John Wiley and Sons, New York, 2013).